Applied Ocean Research 99 (2020) 102124

Contents lists available at ScienceDirect

Applied Ocean Research

journal homepage: www.elsevier.com/locate/apor

Numerical simulations of flow around two tandem wall-mounted structures at high Reynolds numbers

Guang Yin, Martin Andersen, Muk Chen Ong*

Department of Mechanical and Structural Engineering and Material Sciences, University of Stavanger, Stavanger, Norway

A B S T R A C T

In the present study, the flow around two-dimensional (2D) square and trapezoidal wall- mounted structures in tandem on a horizontal flat wall has been simulated using two-dimensional Reynolds-averaged Navier-Stokes (RANS) equations combined with the standard $k-\omega$ SST turbulence model. The Reynolds number (Re) based on the free stream velocity and the height of the structures is set to be 1.19×10^5. The effects of the gap ratio between the two structures as well as the slope angles of the two sides of the trapezoidal structures on the hydrodynamic quantities and the flow around the two structures have been investigated and discussed.

1. Introduction

Flow over wall-mounted structures on a flat wall has been studied through experiments and numerical simulations due to its wide applications in industries. For example, in subsea engineering, the wall-mounted square and trapezoidal ribs have been used as protections over many subsea installations to prevent the damage caused by dropped objects and fishing gears. It is important to investigate the hydrodynamic characteristics of the flow over the subsea covers since the current and wave loads are relevant to their on-bottom stability. In the subsea environments, the extreme currents result in complex turbulent flow at high Reynolds numbers around the wall-mounted structures. The flow characteristics are usually associated with various parameters such as Re (defined as $Re = U_\infty D/\nu$ where D is the height of the structures, U_∞ is the free stream velocity, and ν is the kinematic viscosity), the inflow boundary layer thickness and the characteristic sizes of the structures. As a result, the forces on the structures are difficult to obtain through analytical solutions. Therefore, it is necessary to carry out experiments and numerical simulations to study the hydrodynamic quantities of the flow around the wall-mounted structures.

There are numerous studies of the flow around wall-mounted structures at high Re. Arie et al. [1] studied the pressure distribution around a rectangular cylinder on the wall subjected to a boundary layer flow with different boundary layer thickness and it was found that the drag coefficient decreased with the increasing boundary layer thickness. Good and Joubert [7] conducted experiments on the flow around a wall-mounted bluff-plate in a boundary layer flow and the measurements show that the drag coefficient varies logarithmically with the height of the plate. Martinuzzi and Tropea [13] studied the flow pattern around wall-mounted prismatic obstacles with different aspect ratios W/D (W is the spanwise width of the prismatic structures and D is the height of the structures) in a fully developed turbulent channel flow using experiments. It was found that for the large aspect ratio of $W/D >$ <number>[Numerica]</number>6, the middle region of the wake is two-dimensional while the flow in the separation region in front of the structure is inherently three-dimensional. Bergeles and Athanassiadis [3] investigated experimentally the recirculation region around a two-dimensional obstacle with different aspect ratios and showed that the length of the upstream recirculation length of the obstacle remains unchanged with W/D. However, the length of the downstream recirculation length of the obstacle varies linearly with the aspect ratios of the obstacle. Liu et al. [12] studied the spatial-temporal properties of the separated and reattaching turbulent flows over a two-dimensional (2D) square rib at $Re = 1.32 \times 10^4$ with a boundary layer thickness of $\delta/D = 0.75$ in a wind tunnel. The pressure and velocity fluctuations were measured, and the dominant frequency of the fluctuations was determined. The study also showed that the reattachment point on the bottom wall of the separated shear layer from the leading edge of the rib oscillates with the frequency of the fluctuating velocity and pressure.

Apart from experiments, numerical simulations have been carried out on the turbulent flow around wall-mounted structures. Benodekar et al. [2] carried out numerical simulations of turbulent flow over wall-mounted ribs and the predictions agreed well with the experimental measurements reported by Good and Joubert [7]. Hwang et al. [9] used the standard $k-\varepsilon$ turbulence model to study the flow past a wall-mounted 2D rib with different lengths. It was found that the length of the recirculation region behind the structure decreases linearly with the increasing obstacle length and then remains constant when the reattachment of flow takes place on top of the obstacle. Ryu et al. [19]

* Corresponding author.
E-mail address: muk.c.ong@uis.no (M.C. Ong).

https://doi.org/10.1016/j.apor.2020.102124
Received 2 September 2019; Received in revised form 24 February 2020; Accepted 16 March 2020
Available online 18 April 2020

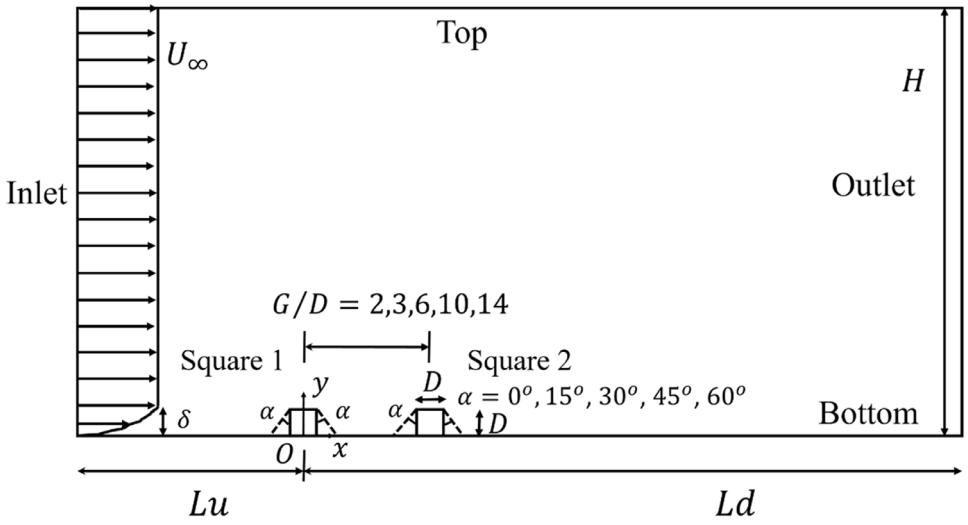

Fig. 1. Computational domain and boundary conditions.

Table 1
Results of convergence study for hydrodynamic coefficients for Squares 1 and 2.

Cases	Cells	G/D	C_{D1}	C_{L1}	C_{D2}	C_{L2}
A1	33,005	2	1.118	0.706	−0.183	0.587
A2	54,135	2	1.112	0.717	−0.194	0.581
A3	72,895	2	1.109	0.721	−0.197	0.578
A4	104,838	2	1.105	0.719	−0.196	0.574
B1	37,139	3	1.134	0.755	−0.286	0.536
B2	60,495	3	1.126	0.762	−0.296	0.527
B3	116,138	3	1.116	0.758	−0.290	0.521
C1	42,219	6	1.150	0.718	−0.458	0.282
C2	66,855	6	1.138	0.716	−0.446	0.279
C3	134,218	6	1.132	0.711	−0.437	0.281
D1	49,839	10	1.061	0.625	−0.215	0.138
D2	76,395	10	1.051	0.621	−0.212	0.137
D3	156,818	10	1.045	0.618	−0.213	0.135
E1	55,681	14	1.026	0.581	−0.012	0.129
E2	92,136	14	1.025	0.580	−0.010	0.129
E3	176,018	14	1.021	0.584	−0.013	0.130

conducted numerical simulations based on Reynolds-averaged Navier-Stokes equations (RANS) with the $k-\omega$ turbulence model to investigate the turbulence characteristics of the flow around 2D wall-mounted structures. The forces exerted on the structures with different shapes by the flow were obtained. Tauqueer et al. [20] carried out 2D RANS simulations on the flow around square, triangular and semi-circular wall-mounted structures using the standard $k-\varepsilon$ model at a high Reynolds number of $Re = 1.0 \times 10^6$. The resulting horizontal velocity profiles showed a good agreement with the experimental measurements performed by Liu et al. [12] and the effects of the boundary layer thickness on the hydrodynamic quantities were discussed. Large eddy simulations (LES) coupling with a finite element method and a boundary element method were carried out by Young et al. [23] to study the flows over a 2D square rib and a 3D cube at $Re = 4.2 \times 10^5$. The model was able to give reasonable prediction results.

Most of the previous researchers studied the flow around a single wall-mounted structure. However, few have investigated the flow characteristics around two tandem structures, which may display different hydrodynamic features. Dai et al. [6] performed 2D RANS simulations with the standard $k-\omega$ turbulence model to investigate the drag and lift force coefficients of two squares in tandem as well as the velocity contours and pressure contours around them at the low Reynolds number of $Re = 4000$. In the present study, RANS simulations with the $k-\omega$ SST model are carried out to obtain the hydrodynamic quantities such as drag coefficient, lift coefficient for two symmetric trapezoidal wall-mounted structures in tandem with different incline

Table 2
Hydrodynamic coefficients for Structures 1 and 2 with $G/D = 6$ for trapezoidal configurations using the grid resolution of Case C2 in Table 1.

α	C_{D1}	C_{L1}	C_{D2}	C_{L2}
0	1.138	0.716	−0.446	0.279
15	1.106	0.605	−0.434	0.387
30	1.104	0.533	−0.415	0.435
45	0.934	0.479	−0.382	0.450
60	0.728	0.443	−0.253	0.442

Table 3
Hydrodynamic coefficients for Structures1 and 2 with $G/D = 10$ for trapezoidal configurations using the grid resolution of Case D2 in Table 1.

α	C_{D1}	C_{L1}	C_{D2}	C_{L2}
0	1.051	0.621	−0.212	0.137
15	1.023	0.504	−0.198	0.206
30	0.969	0.421	−0.172	0.249
45	0.864	0.366	−0.119	0.274
60	0.671	0.335	−0.014	0.284

angles of the two side slopes at $Re = 1.19 \times 10^5$. Effects of the gap ratio between the two structures and the incline angle of two side slopes of the trapezoidal structures on the hydrodynamic quantities and the flow characteristics around the two structures are investigated. Other studies on the flow past tandem structures include Paik et al. [16] where detached eddy simulations (DES) were carried out on the flow over two tandem wall-mounted cubes at $Re = 2 \times 10^4$, Wang et al. [21] where experiments were conducted to investigate the flow characteristics around two near-wall tandem squares at $Re = 6300$. Gopalan and Jaiman [8] where hybrid RANS-LES was used to simulate the flow around two tandem cylinders at $Re = 1.66 \times 10^5$ and Prsic et al. [17, 18], Li et al. [11] where LES was carried out to study the flow over two tandem cylinders near a flat wall at $Re = 1.31 \times 10^4$.

The paper is organized as follows. First, the mathematical formulation and the numerical methods are given in Section 2. The grid resolution studies, the validation studies as well as the results and discussion are presented in Section 3. Finally, conclusions are given.

2. Mathematical formulation

2.1. Flow model

The Reynolds-averaged equations for the conservation of mass and momentum for steady-state turbulent flow are presented as follows:

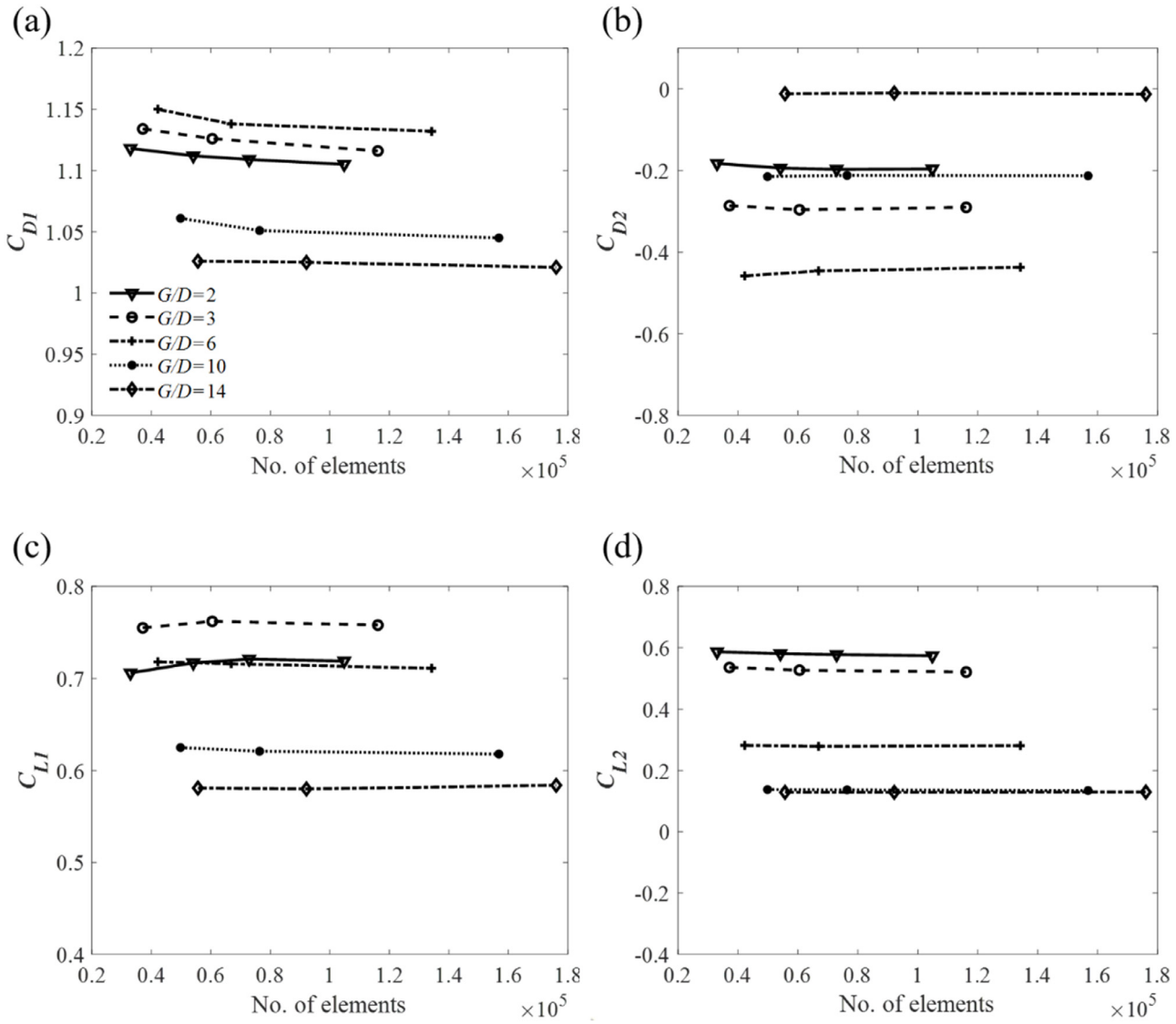

Fig. 2. Convergence study for wall-mounted squares in tandem with G/D = 2, 3, 6, 10 and 14 for the hydrodynamic quantities: (a) C_{D1} for Square1; (b) C_{D2} for Square2; (c) C_{L1} for Square1 and (d) C_{L2} for Square2.

$$\frac{\partial u_i}{\partial x_i} = 0 \tag{1}$$

$$u_j \frac{\partial u_i}{\partial x_j} = -\frac{1}{\rho}\frac{\partial P}{\partial x_i} + \nu \frac{\partial^2 u_i}{\partial x_j^2} - \frac{\partial \overline{u_i' u_j'}}{\partial x_j} \tag{2}$$

where $i, j = 1, 2$ (for x, y) denote the streamwise and cross-stream directions, respectively; u_1 and u_2 (for u and v) are the corresponding mean velocity components. $\overline{u_i' u_j'}$ is the Reynold stress component where u_i' represents the fluctuating part of the velocity; P is the mean pressure; and ρ is the fluid density.

The Reynolds stress component is represented based on a turbulent viscosity ν_T and the gradients of the mean flow according to the Boussinesq approximation as

$$\overline{-u_i' u_j'} = \nu_T \left(\frac{\partial u_i}{\partial x_j} + \frac{\partial u_j}{\partial x_i} \right) - \frac{2}{3} k \delta_{ij} \tag{3}$$

where k is the turbulent kinetic energy and δ_{ij} is the Kronecker delta function.

The $k-\omega$ SST turbulence model [14] is employed in the present study. The SST model is a combination of the $k-\omega$ and the $k-\varepsilon$ models. The near wall region of the domain is treated with the $k-\omega$ model of Wilcox [22] while the standard $k-\varepsilon$ model of Jones and Launder [10] is used in the outer wake region and in the free shear layers. According to Menter et al. [24], the equations of k and ω can be expressed as follows:

$$\frac{Dk}{Dt} = \widetilde{P_k} - \beta^* \omega k + \frac{\partial}{\partial x_j}\left[(\nu + \sigma_k \nu_t) \frac{\partial k}{\partial x_j} \right] \tag{4}$$

$$\frac{D\omega}{Dt} = \alpha S^2 - \beta \omega^2 + \frac{\partial}{\partial x_j}\left[(\nu + \sigma_\omega \nu_t) \frac{\partial \omega}{\partial x_j} \right] + 2(1 - F_1)\sigma_{\omega 2} \frac{\partial k}{\partial x_j}\frac{\partial \omega}{\partial x_j} \tag{5}$$

where $\widetilde{P_k}$ is expressed by

$$\widetilde{P_k} = min\left[\nu_t \frac{\partial u_i}{\partial x_j}\left(\frac{\partial u_i}{\partial x_j} + \frac{\partial u_j}{\partial x_i} \right), 10\beta^* \omega k \right] \tag{6}$$

Φ_1 represents any constant in the original $k-\omega$ model (σ_{k1}, …) and Φ_2 represents any constant in the original $k-\varepsilon$ model (σ_{k2}, ..). Then the constant Φ of the new model is denoted as

$$\Phi = F_1 \Phi_1 + (1 - F_1)\Phi_2 \tag{7}$$

$$F_1 = \tanh(arg_1^4) \tag{8}$$

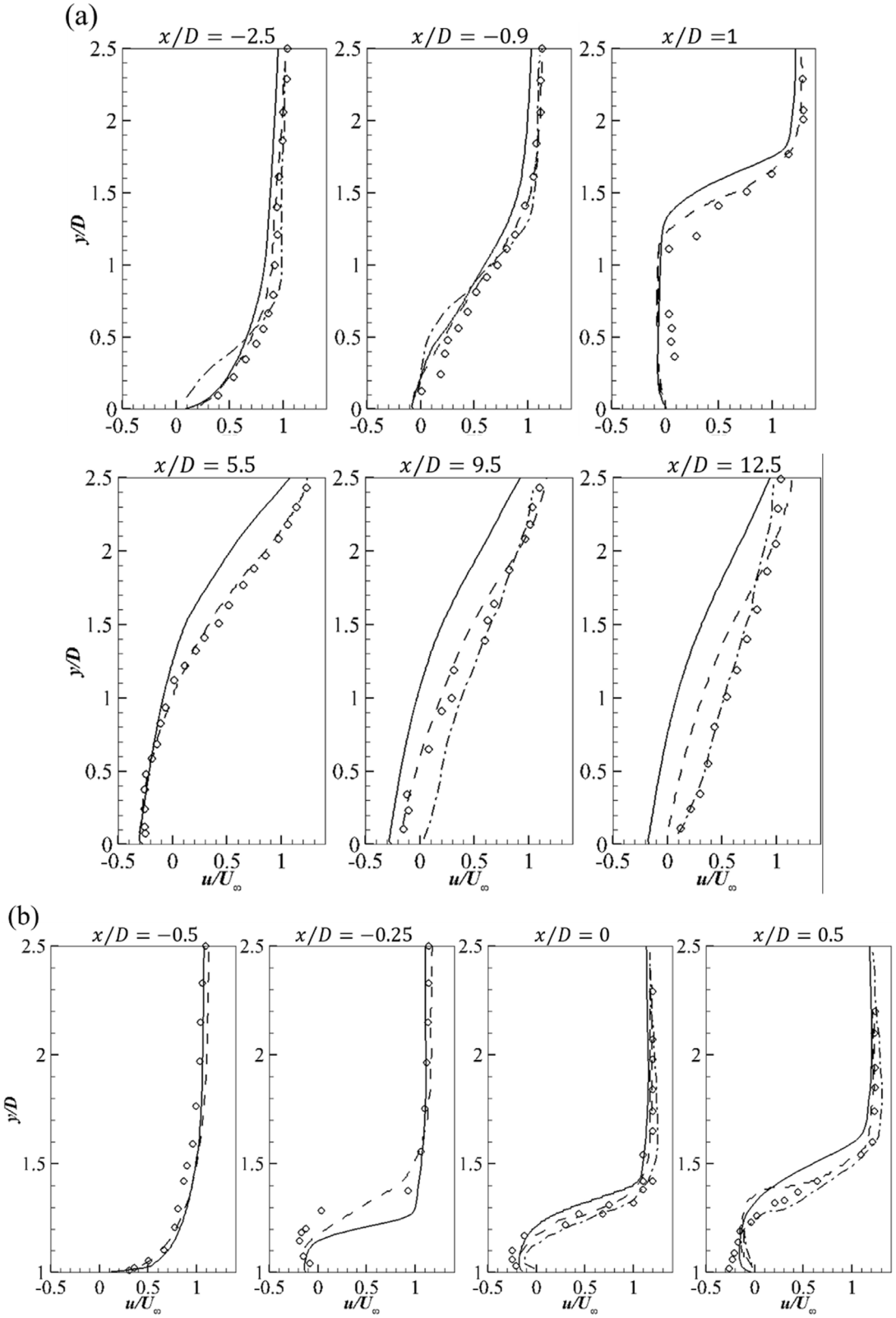

Fig. 3. Streamwise velocity profiles in the present study at $Re = 4.2 \times 10^5$(solid lines) compared with the experimental data (Circles: [5]) and the numerical results (Dashes: [2]; Dashes: [23]) (a) in front of and downstream of the square; (b) on the top of the square. linesedictions and measurements downstream of the square.

$$arg_1 = \min\left[\max\left(\frac{\sqrt{k}}{\beta^* \omega y}, \frac{500\nu}{y^2\omega}\right)\frac{4\rho\sigma_{\omega 2}k}{CD_{k\omega}y^2}\right] \tag{9}$$

$$CD_{k\omega} = \max\left(2\rho\sigma_\omega \frac{1}{\omega}\frac{\partial k}{\partial x_j}\frac{\partial \omega}{\partial x_j}, 10^{-10}\right) \tag{10}$$

where y is the distance to the closest wall. $CD_{k\omega}$ is the positive portion of the cross-diffusion term in (4).

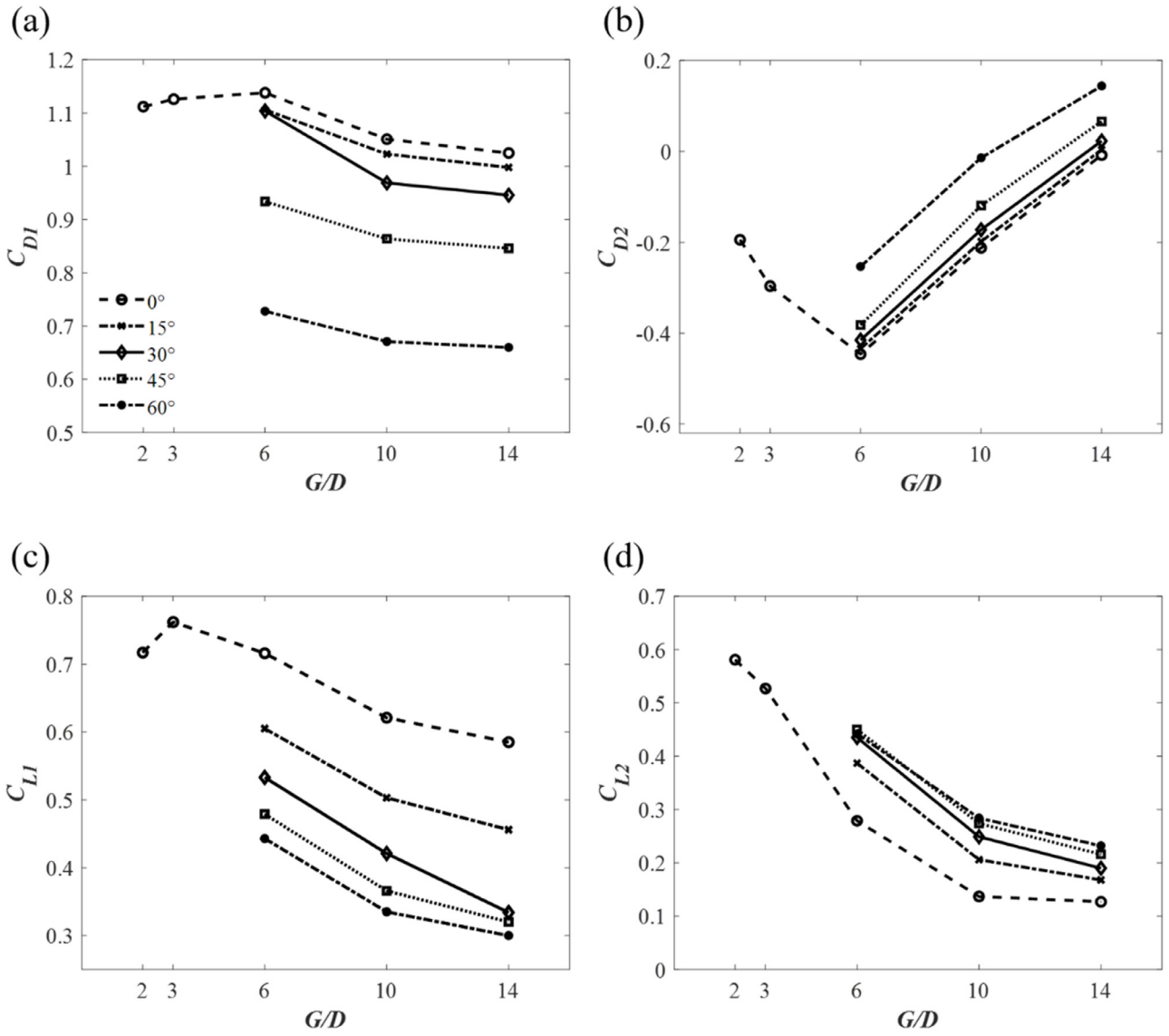

Fig. 4. Variations of the hydrodynamic quantities with G/D for different α: (a) C_{D1} for Square 1; (b) C_{D2} for Square 2; (c) C_{L1} for Square 1; (d) C_{L2} for Square 2.

The turbulent eddy viscosity is defined as

$$\nu_t = \frac{a_1 k}{\max(a_1\omega, SF_2)} \tag{11}$$

where S is the invariant measure of the strain rate and F_2 is

$$F_2 = \tanh(arg_2^2), \tag{12}$$

$$arg_2 = \max\left(2\frac{\sqrt{k}}{0.09\omega y}, \frac{500\nu}{y^2\omega}\right) \tag{13}$$

The SST constants are: $\beta^* = 0.09$, $\alpha_1 = 0.5532$, $\alpha_2 = 0.4403$, $\beta_1 = 0.075$, $\beta_1 = 0.0828$, $\sigma_{k2} = 1.0$ and $\sigma_{\omega 1} = 0.5$, $\sigma_{\omega 2} = 0.85616$.

2.2. Computational domain and boundary conditions

OpenFOAM, an open source computational fluid dynamic (CFD) code based on the finite volume method, is used to solve the RANS equations for the conservation of mass and momentum in the present study. A solver based on a semi-implicit method for pressure linked equations (SIMPLE), simpleFoam is used. The spatial schemes for gradient, Laplacian and divergence are Gauss linear, bounded Gauss linear upwind, and Gauss linear limited corrected.

Fig. 1 presents the 2D computational domain used in the present study for the two structures in tandem. The origin of the coordinates is located at the bottom center of the first wall-mounted structure. The height and top lengths of the two structures is D and the inclined angles of the trapezoidal structures are $90° - \alpha$, i. e. ,90°(square), 75°, 60°, 45° and 30°. The distance between the centers of the bottom edges of the two structures is denoted as G. The height of the rectangular computational domain is $20D$, which is larger than the height of $17D$ in the experimental data reported by Arie et al. [1]. The flow inlet boundary is located Lu upstream from the center of the bottom edge of the first structures and the flow outlet boundary is located Ld downstream from the center of the bottom edge of the first structure. The value of Lu is set to be $11.5D$. This length is larger than that used in Ong et al. [15], where the flow around a cylinder close to a flat wall is simulated with the inlet length of $10D$. In the present study, prior studies have been carried out to determine the value of Ld. For the largest value of $G/D = 14$, when Ld is increased from 40.5D to 60.5D, the maximum relative change of the hydrodynamic quantities is 5.8%. If Ld is increased further from 60.5D to 80.5D, the maximum change in the hydrodynamic quantities is negligible. Therefore, for the cases with $G/D = 14$, $Ld = 60.5D$ is used. For other G/D, $Ld = 40.5D$ is used where the largest distance between the outlet and Structure 2 is $30.5D$. This

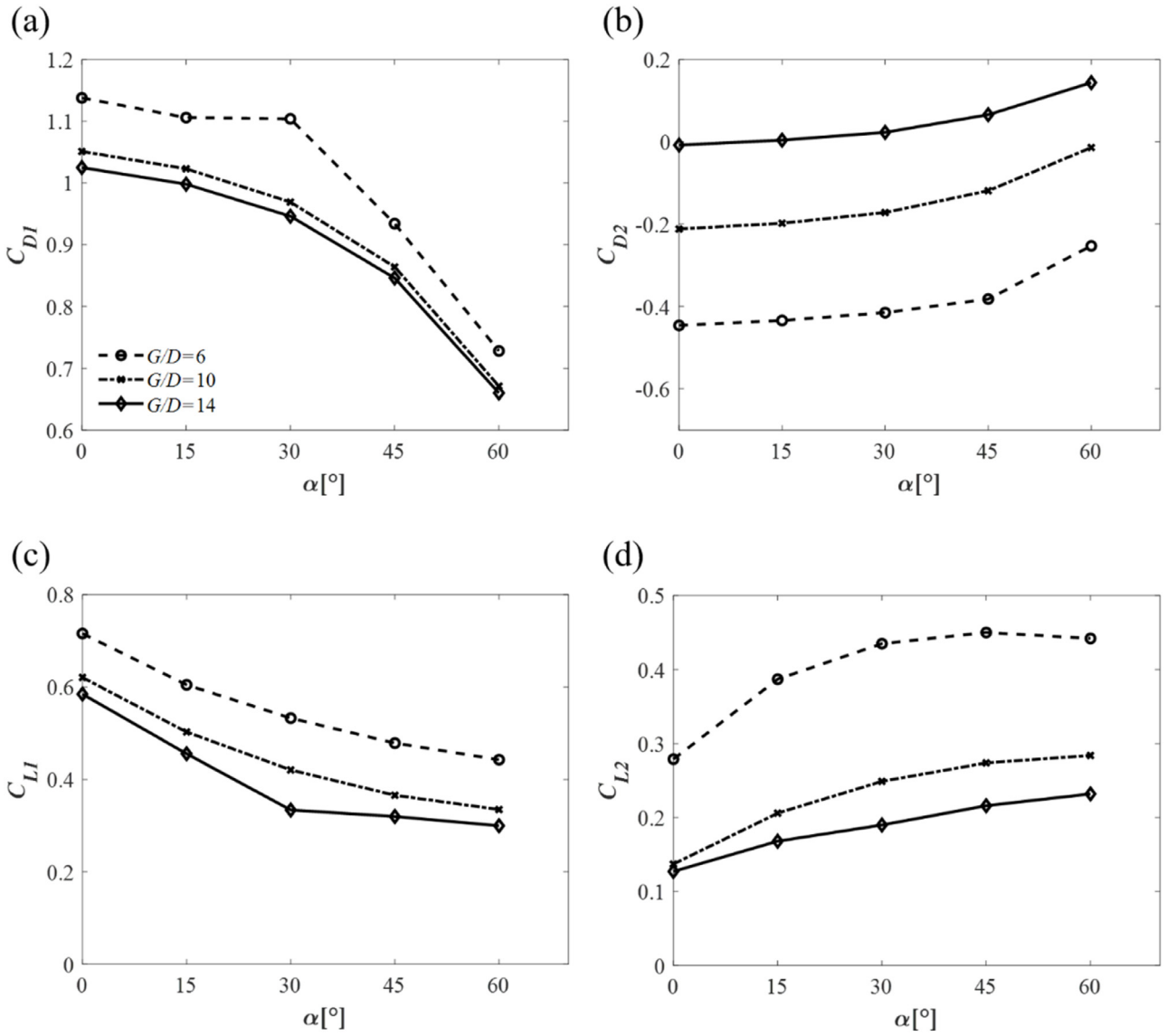

Fig. 5. Variations of α on the hydrodynamic quantities with G/D = 6, 10, 14: (a) C_{D1} for Structure 1; (b) C_{D2} for Structure 2; (c) C_{L1} for Structure 1; (d) C_{L2} for Structure 2.

length is larger than that used in the previous studies carried out by Young et al. [23] (20D), Prisic et al. [18] (30D) and Li et al. [11] (30D). Therefore, it can be ensured that the domain is large enough to suppress any far-field effects on the structures. The boundary conditions for the simulations are set as follows:

The inlet velocity is a turbulent boundary layer flow, with a logarithmic horizontal velocity u_1 profile adapted from the experiments done by Arie et al. [1] to ensure similarity to the experimental set up for comparisons. The vertical velocity is set to be $u_2 = 0$. This velocity profile is used throughout the study. The value of k and ω is given as follows:

$$k(y) = \max\left\{C_\mu^{-\frac{1}{2}}\left(1-\frac{y}{\delta}\right)\times\left|1-\frac{y}{\delta}\right|u^{*2}, 0.0001U_\infty^2\right\} \tag{14}$$

$$\omega = \frac{k^{0.5}}{C_\mu^{0.5} l} \tag{15}$$

$$l = \min\left\{\kappa y\left(1+3.5\frac{y}{\delta}\right)^{-1}, C_\mu\delta\right\} \tag{16}$$

where $C_\mu = 0.09$ is the turbulent-viscosity constant, u^* is the bottom wall friction velocity, $\kappa = 0.41$ is the Karman constant and l is the turbulent length scale (see e.g., [4, 15]). The boundary layer thickness is set to be a fixed value of $\delta/D = 0.73$ which is the same as that reported by Arie et al. [1].

No-slip condition ($u_1 = u_2 = 0$) and standard near-wall conditions for k and ω is applied on the surface of the structures and the bottom wall where $y^+ > 30$ is satisfied and y^+ is given as:

$$y^+ = \frac{\Delta y u^*}{\nu} \tag{17}$$

where Δy is the distance of the center of the first grid away from the wall.

At the outlet, u_1, u_2, k and ω are specified as zero normal gradient and the pressure is set be zero.

At the top, u_1, u_2, k and ω are set as zero normal gradient.

3. Results and discussion

3.1. Grid resolution studies and validation studies

A grid convergence study is performed for the flow at

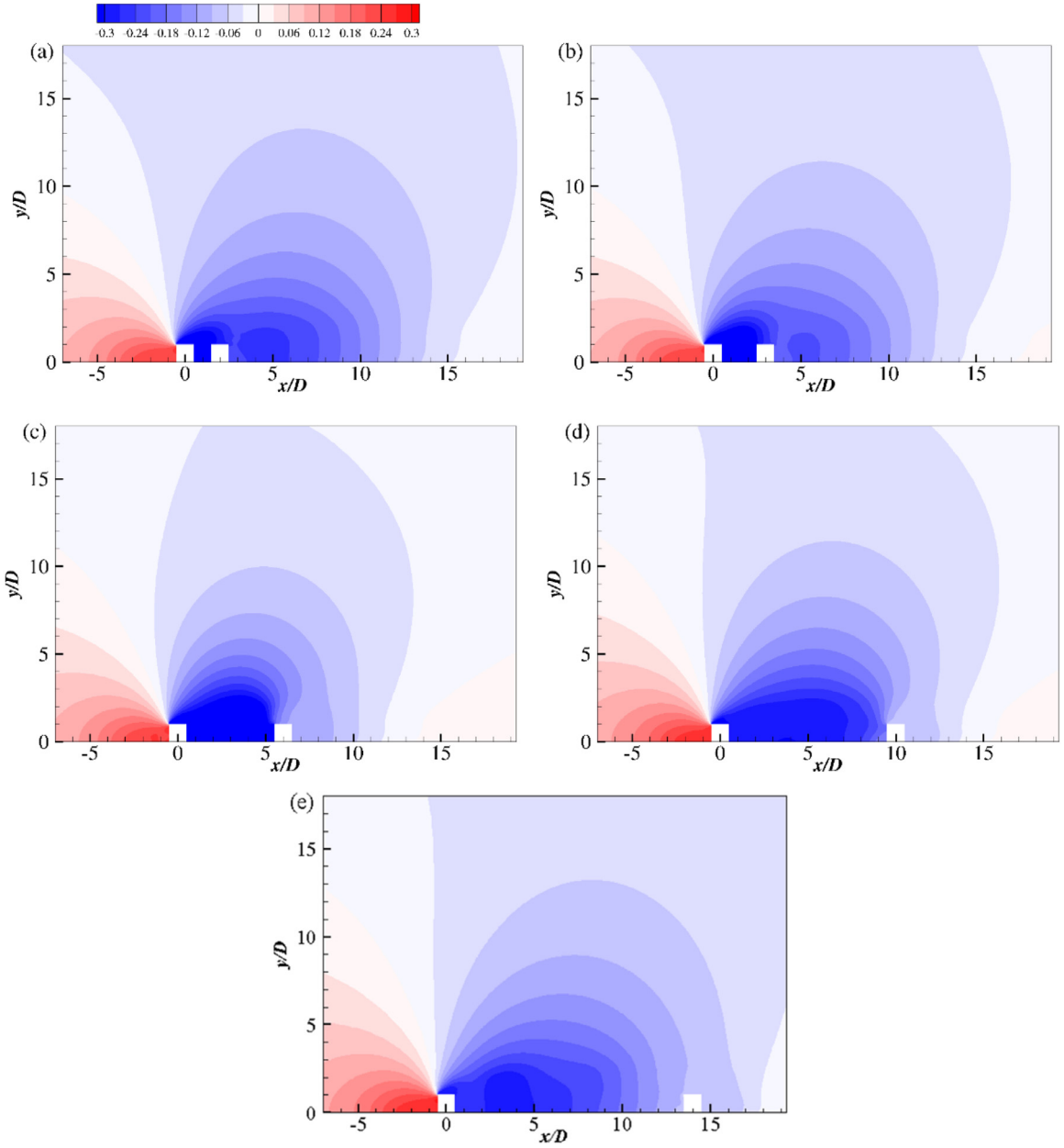

Fig. 6. Pressure contours ($2p/\rho U_\infty^2$) for wall-mounted squares in tandem with: (a) $G/D = 2$; (b) $G/D = 3$; (c) $G/D = 6$; (d) $G/D = 10$; (e) $G/D = 14$.

$Re = 1.19 \times 10^5$ with 3 sets of meshes (from coarse to dense) for each G/D between the two squares ('Square 1' and 'Square 2' are used when referring to the first and second square configurations in tandem, respectively) as shown in Table 1 to determine the resolutions of the grid for all the simulations in the present study. The hydrodynamic coefficients such as the drag coefficients (defined as $C_D = 2F_D/(\rho D U_\infty^2)$ where F_D is the steady state drag force acting on the structures per unit length in the streamwise direction, ρ is the density of the fluid and U_∞ is the free stream velocity of the boundary layer flow as shown in Fig. 1) and the lift coefficients (defined as $C_L = 2F_L/(\rho D(1 + 2\tan\alpha)U_\infty^2)$ where F_L is the steady state lift force acting on the structures per unit length in the cross-stream direction and $D(1 + 2\tan\alpha)$ is the bottom length of the structures) on the two structures (denoted as C_{D1}, C_{L1} and C_{D2}, C_{L2} for Square 1 and Square 2 respectively). Fig. 2 shows the variations of the hydrodynamic quantities with the grid numbers. It can be seen that the variations of C_{D1}, C_{D2}, C_{L1} and C_{L2} between cases A2, B2, C2, D2, E2 and A4, B3, C3, D3, E3 with the finest meshes are within 5%. As a result, the meshes of A2~E2 for each G/D can provide sufficient resolutions and their resolutions are also used for the two trapezoidal structures with $G/D \geq 6$ as shown in Tables 2, 3 and 4. In the present study, simulations with $G/D < 6$ are not carried out for trapezoids in tandem because of the high skewness of the meshes located between the two trapezoidal structures when $\alpha > 30°$.

In order to validate the present numerical model, simulations of flow around a single wall-mounted square at $Re = 1.19 \times 10^5$ has been carried out and compared with the experimental data reported by Arie et al. [1] under the same flow condition. The grid resolution of Case A2 in Table 1 is used and the resulting drag coefficient is $C_D = 1.00$, which is in a good agreement with the experimental data reported by Arie et al. [1] ($C_D = 0.96$) at the same Re. Additional simulations are carried out at $Re = 4.2 \times 10^5$ and the results are compared with the experimental data reported by Crabb et al. [5], the simulation results reported by Benodekar et al. [2] and Young et al. [23] at the same Re. The gird convergence studies are carried out and the value of C_D and C_L are shown in Table 5. By comparing the results of Cases E2 and E3, the relative difference of C_D is 0.89% and the relative difference of C_L is

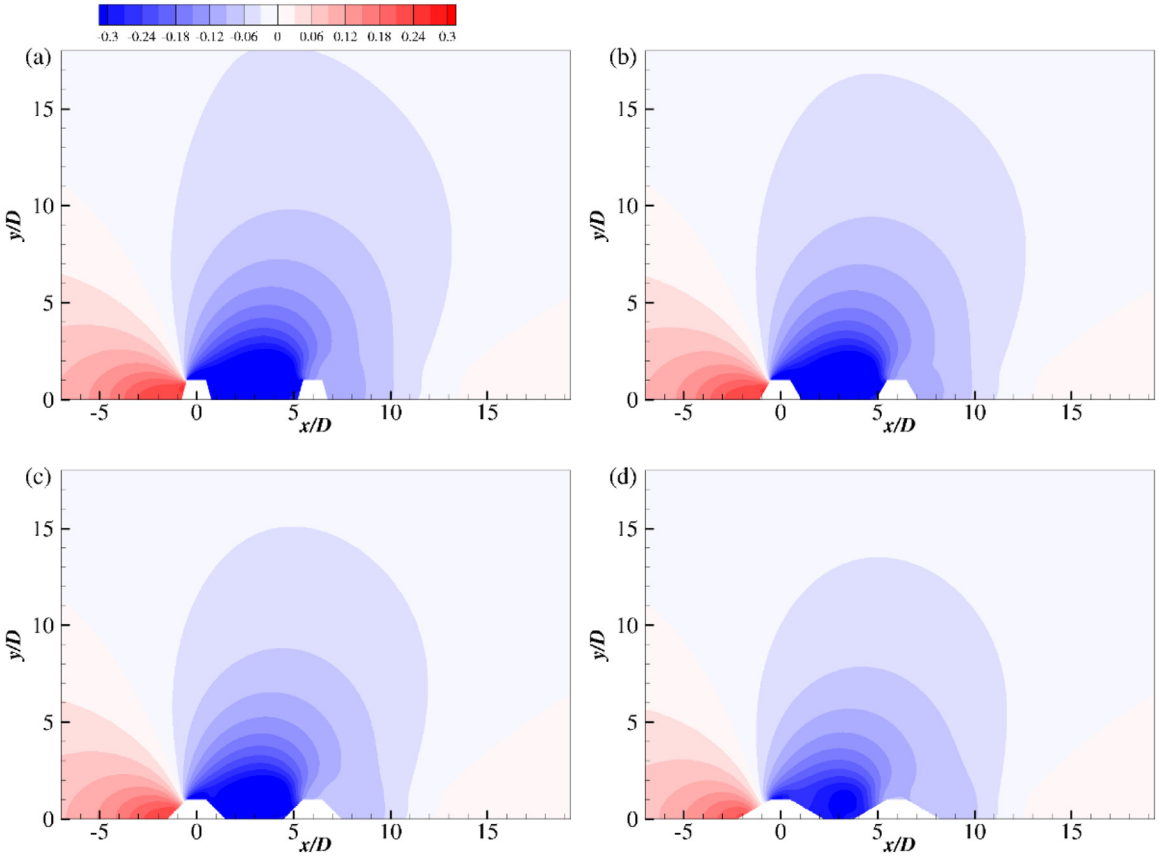

Fig. 7. Pressure contours ($2p/\rho U_\infty^2$) with $G/D = 6$ for different α: (a) 15°; (b) 30°; (c) 45°; (e) 60°.

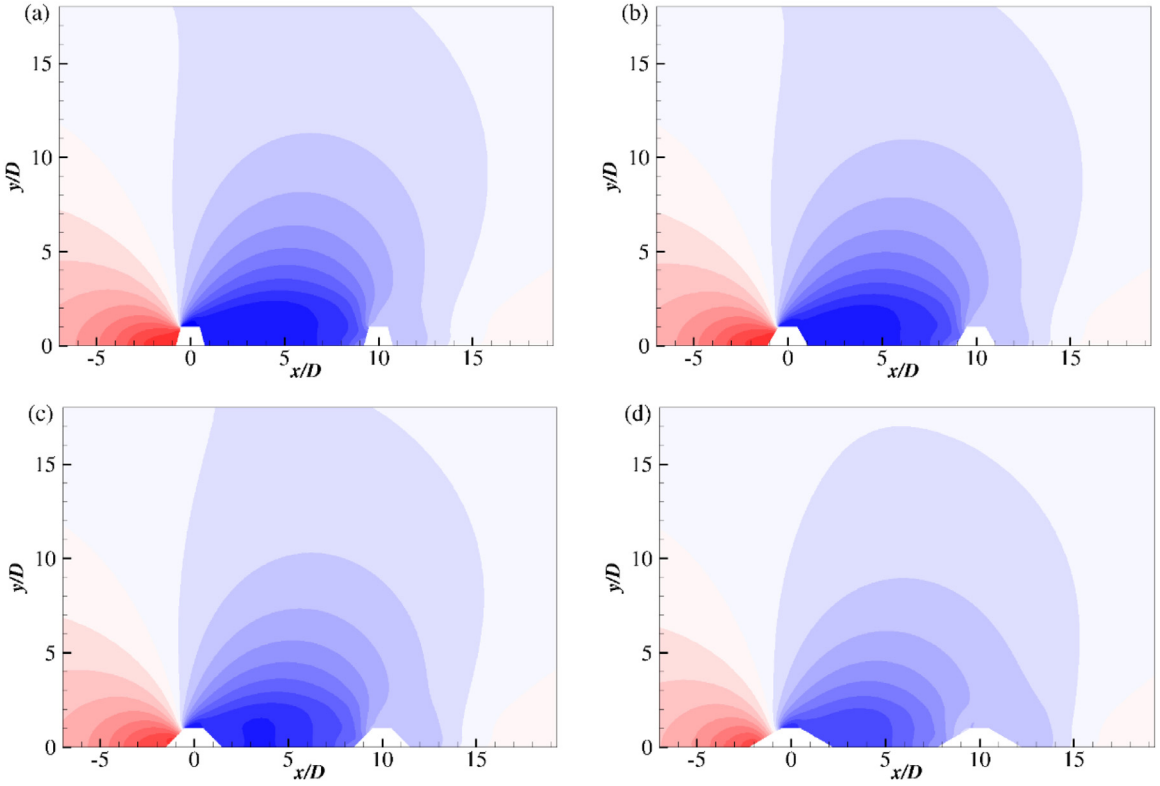

Fig. 8. Pressure contours ($2p/\rho U_\infty^2$) with $G/D = 10$ for different α: (a) 15°; (b) 30°; (c) 45°; (e) 60°

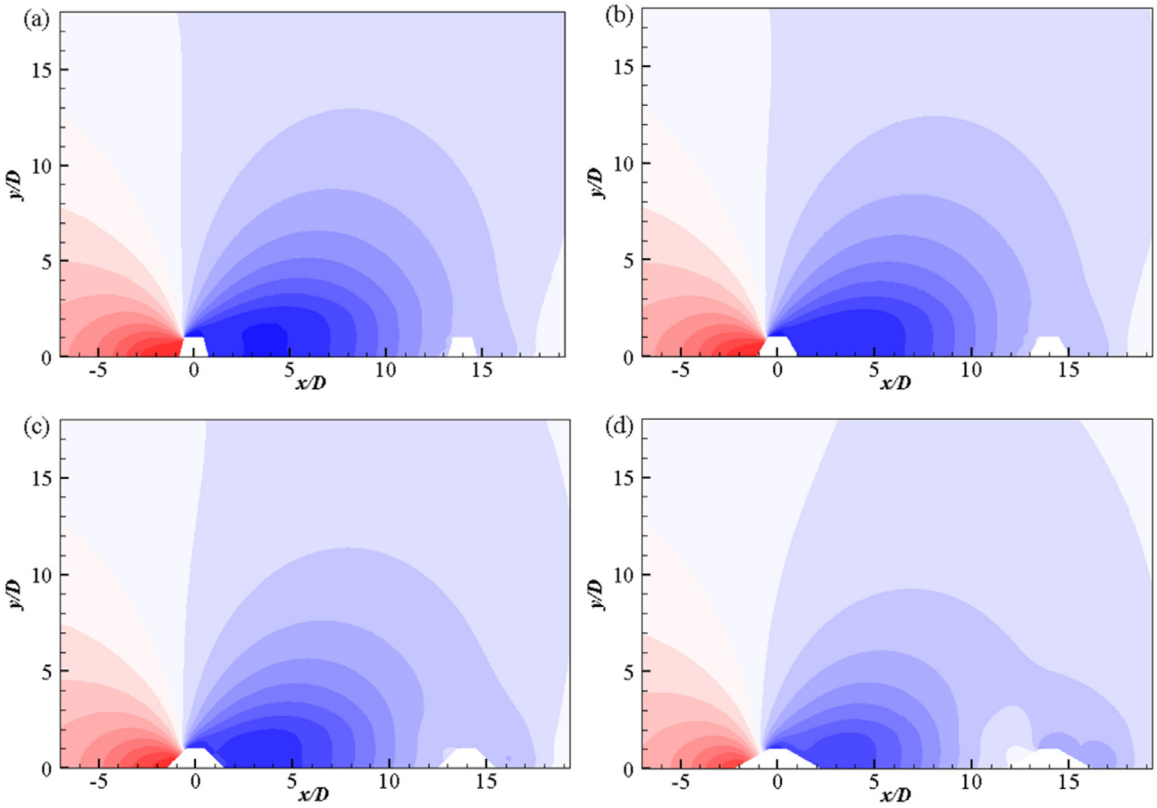

Fig. 9. Pressure contours ($2p/\rho U_\infty^2$) with $G/D = 14$ for different α: (a) 15°; (b) 30°; (c) 45°; (e) 60°

Table 4
Hydrodynamic coefficients for Structures1 and 2 with $G/D = 14$ for trapezoidal configurations using the grid resolution of Case E2 in Table 1.

α	C_{D1}	C_{L1}	C_{D2}	C_{L2}
0	1.025	0.585	−0.008	0.127
15	0.998	0.456	0.004	0.168
30	0.946	0.334	0.023	0.190
45	0.846	0.320	0.066	0.216
60	0.660	0.300	0.144	0.232

Table 5
Results of convergence study for hydrodynamic coefficients for a single square at $Re = 4.2 \times 10^5$.

Cases	Cells	C_D	C_L
E1	39,360	1.15	0.630
E2	53,124	1.13	0.631
E3	85,824	1.12	0.628

0.48%. Therefore, the meshes of Case E2 can give sufficient grid resolution. The grid resolution of Case E2 in Table 5 is used and the resulting streamwise velocity profiles at different locations around the square are compared with those obtained by the previous published studies by Crabb et al. [5], Benodekar et al. [2] and Young et al. [23]. The streamwise velocity profiles in front of the square and downstream of the square are shown in Fig. 3(a). A good agreement has been achieved in front of the square and at the downstream locations of $x/D = 1$. There is discrepancies at the streamwise locations of $x/D = 9.5, 12.5$. The predicted streamwise velocity profiles on the top the square match well with the previous published results in Crabb et al. [5], Benodekar et al. [2] and Young et al. [23], as shown in Fig. 3(b). In general, the present numerical model can provide reasonable predictions of hydrodynamic quantities on the structures.

3.2. Parametric studies

3.2.1. Effects of G/D on hydrodynamic quantities

Fig. 4 presents the variations of the hydrodynamic quantities for the two structures with different G/D at $Re = 1.19 \times 10^5$. For the square structures, C_{D1} is increasing with $G/D = 2 \sim 6$ but declining with $G/D \geq 6$ as seen in Fig. 4(a). The sign of the drag coefficient is opposite for Square 2 to that for Square 1 as seen in Fig. 4(b). The maximum absolute value for C_{D2} is also found with $G/D = 6$ and then decreases linearly with G/D. The negative drag coefficient of Square 2 can be explained that there is a large low-pressure region formed between the two squares and the amplitude of the low-pressure region is larger than that behind Square 2. This can be further indicated by the pressure contours in following sections. The lift coefficient for Square 1 reaches its maximum value with $G/D = 3$ and monotonically decreases with the increasing G/D. For the trapezoidal structures, both C_{D1} and C_{L1} decrease with $G/D > 6$. With $G/D = 6, 10$, C_{D2} is negative for all α. However, with $G/D = 14$ and $\alpha = 45°, 60°$, C_{D2} becomes positive because for this gap ratio between the two structures, Structures 2 becomes less influenced by the small wake zone of Structure 1. C_{L2} is decreasing with G/D for the square and trapezoids with all α and its variation with G/D tends to be flat with $G/D > 10$.

3.2.2. Effects of α on hydrodynamic quantities

The variations of the hydrodynamic quantities with α are shown in Fig. 5 with $G/D = 6$, 10 and 14. Both C_{D1} and C_{L1} are decreasing with the increasing α. The decreasing C_{D1} in Fig. 5(a) is because the retardation effect of the structure to the flow becomes weak with the increasing α, which results in lower pressure difference between the front and back face of the structure, and hence causes lower drag force on the Structure 1. The decreasing C_{L1} is mainly due to the larger projected area in the vertical direction. From Fig. 5(b), the value of C_{D2} is negative with all α for $G/D = 6$ and 10. However, with $G/D = 14$, C_{D2} is almost zero for the square because Square 2 is placed almost out of

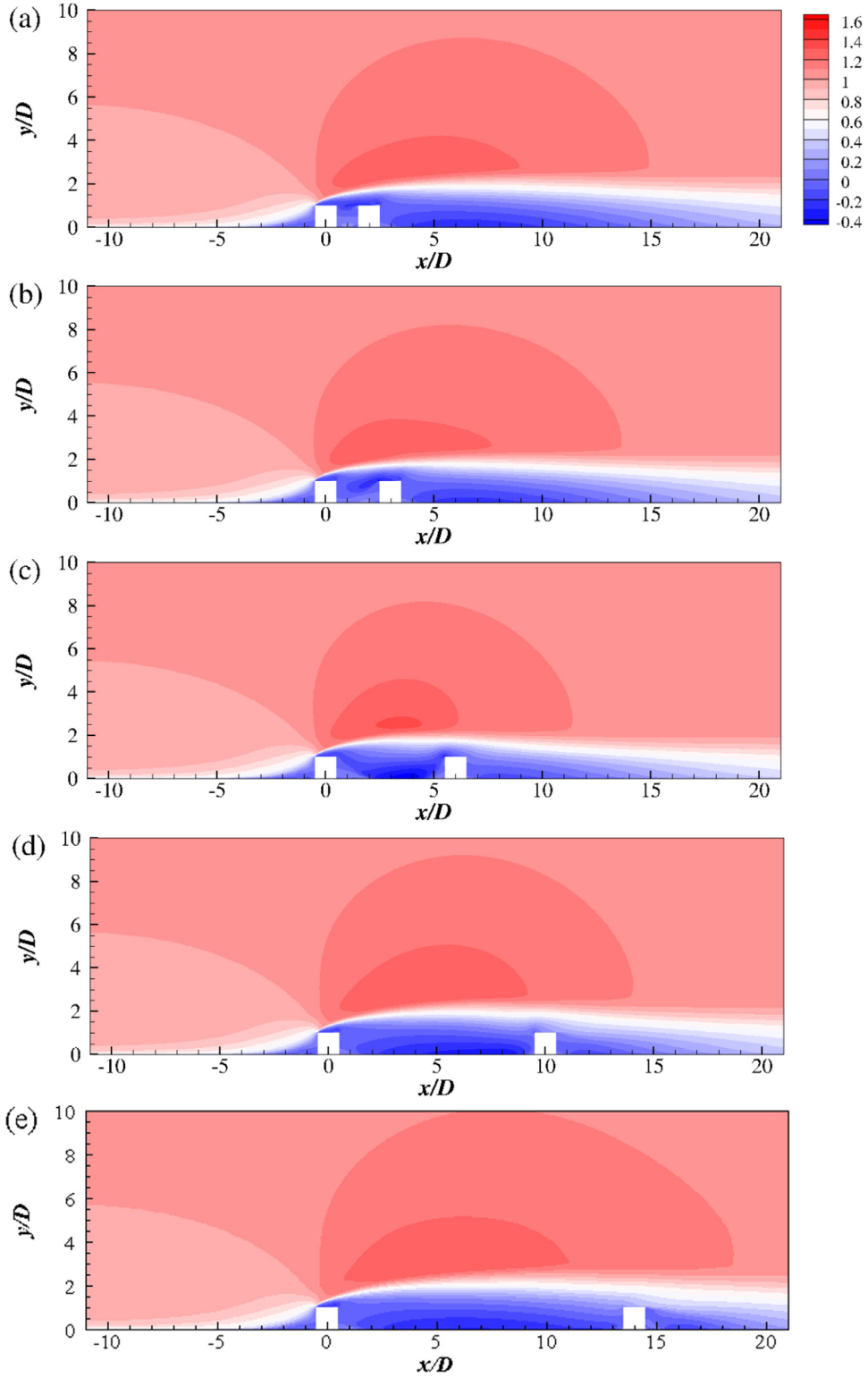

Fig. 10. Horizontal velocity contours (u/U_∞) for wall-mounted squares in tandem with G/D of: (a) $G/D = 2$; (b) $G/D = 3$; (c) $G/D = 6$; (d) $G/D = 10$; (e) $G/D = 14$.

the wake zone of Square 1 and the pressure on the front and back face of Square 2 is nearly identical, which will be further illustrated in the following section. For $G/D = 14$, with the increasing α, C_{D2} becomes positive and increases, which is different from that of Structure 1. This may be due to the reason that the recirculation region behind Structure 1 becomes smaller with the increasing α and the incoming flow to which Structure 2 is subjected tends to recover to the boundary layer flow. As a result, a higher-pressure region is formed in front of Structure 2 with the increasing α, as can also be seen in the pressure distributions in the following section. Furthermore, C_{L2} is positive for all G/D and increases with the increasing α, which is different from C_{L1}. C_{L2} is largest with $G/D = 6$ and reaches its maximum value with $\alpha = 45°$, and then slightly declines with $\alpha = 60°$. For $G/D = 10$ and 14, C_{L2} is increasing with the larger α.

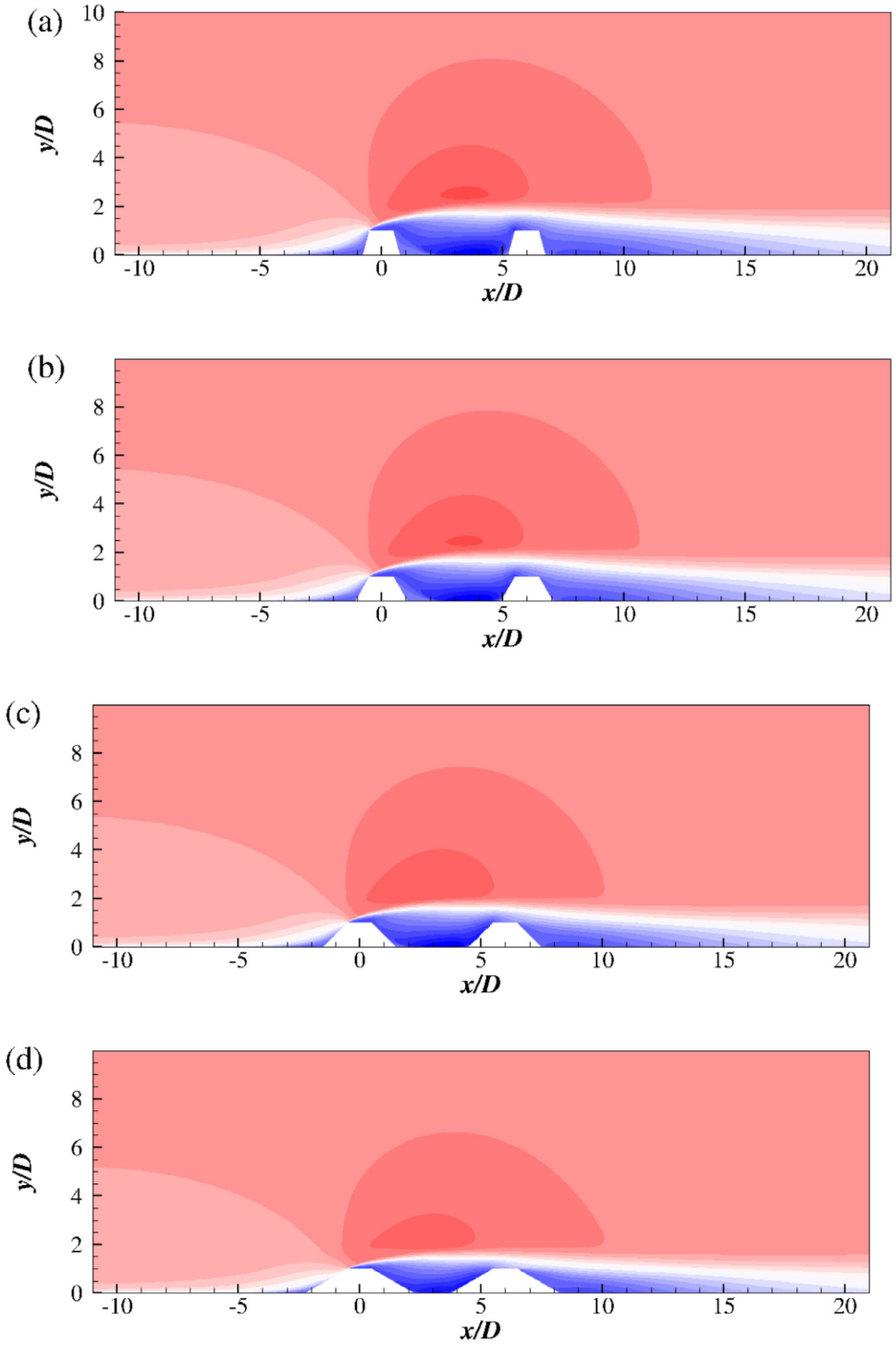

Fig. 11. Horizontal velocity contours (u/U_∞) with $G/D = 6$ for different α : (a) 15°; (b) 30°; (c) 45°; (d) 60°

3.3. Pressure distributions around the structures in tandem

The pressure distributions for $G/D = 2,\ 3,\ 6,\ 10$ and 14 for the two squares and trapezoids in tandem have been investigated and presented in Figs. 6–9.

From the pressure distribution around the two squares, it can be seen that a large positive pressure region is formed around the front face of Square 1 due to the conservation of energy. Furthermore, for all G/D, two negative pressure regions are formed. One is formed between the two squares and the other one is formed behind Square 2. For $G/D = 2 \sim 10$, the amplitude of the negative pressure region between the two squares is lower than that behind Square 2 and because the main contribution of the drag force on the structures comes from the pressure difference between the front and back face of the structures, C_{D2} is negative. Dai et al. [6] has also reported that the pressure region between the structures imposes a suction force on Square 2 with $G/D = 3$. For $G/D = 14$, the pressures around the front and back face of Square 2 are similar, and hence C_{D2} becomes almost zero.

The amplitude of the first negative-pressure zone between the two square increases with $2 < G/D < 6$ and decreases with $6 < G/D < 14$ as indicated in Fig. 6(a)–(e), which is associated with the drag

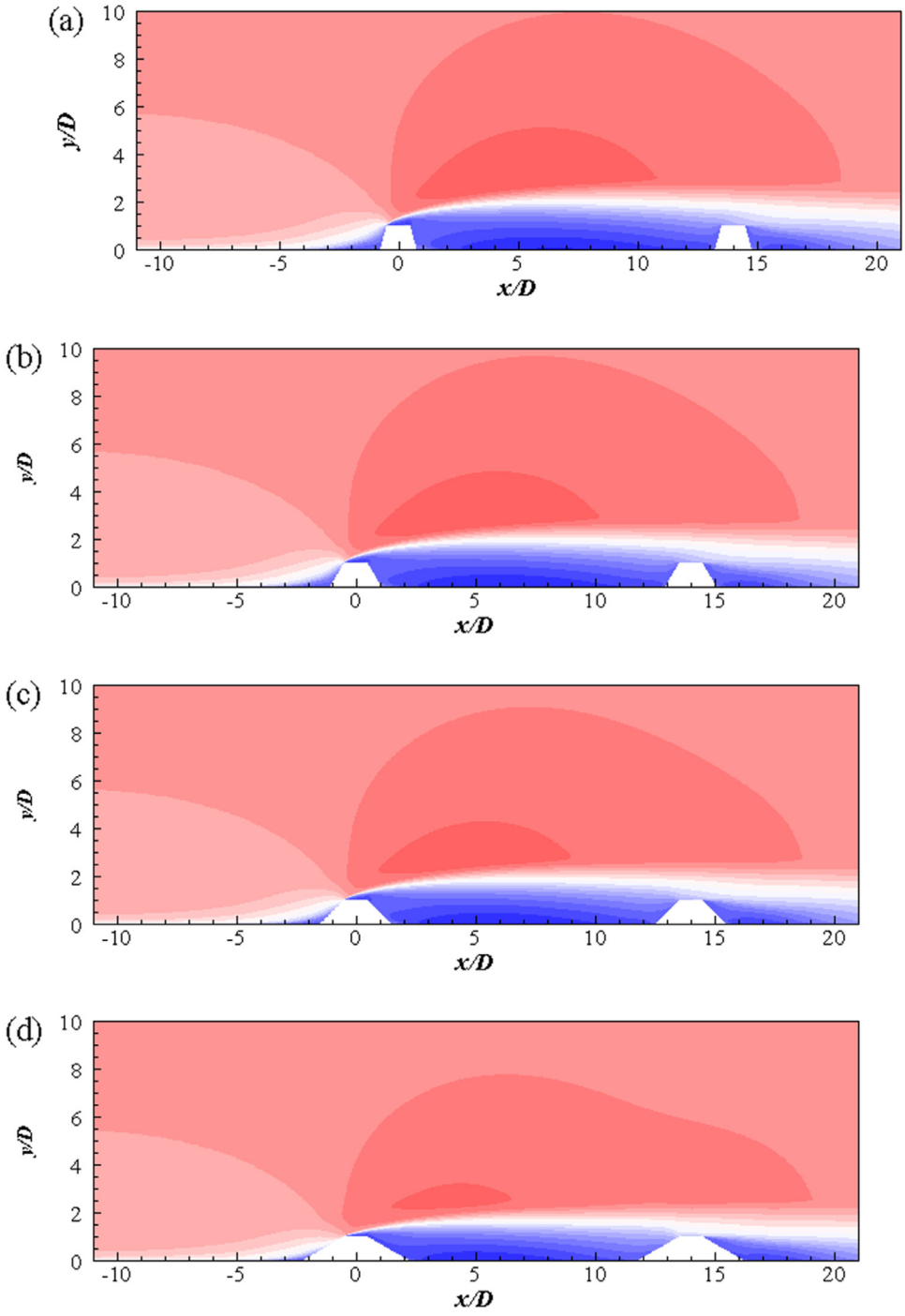

Fig. 12. Horizontal velocity contours (u/U_∞) with $G/D = 14$ for different α : (a) 15°; (b) 30°; (c) 45°; (d) 60°

coefficient variations of Square1 and Square 2 in Fig. 4(a) and (b). The second negative pressure region is formed around $x/D \sim 5$ behind Square 2 as seen in Fig. 6(a) and (b) and disappears in Fig. 6(c)–(e) with $G/D = 10,\ 14$. With $G/D = 6$ where a turning point takes place for C_{D1} and C_{D2}, it seems that the two negative pressure regions are merged and one large negative pressure region is formed between the squares, hence imposing the largest drag forces on the two structures. Moreover, the amplitude of the negative-pressure region between the two structures decreases with $6 < G/D \leq 14$ and seems to be less affected by Square 2 with $G/D \geq 10$.

Figs. 7, 8, 9 show the pressure contours for all trapezoidal structures with $G/D = 6 \sim 14$. The amplitudes of the positive-pressure region at the front face of Structure 1 and the negative-pressure region between the two structures are decreasing with the increasing α. For $G/D = 10,\ 14$, the size of the negative pressure region formed behind Structure 2 is slightly increasing with the increasing α. For $G/D = 14$ and $\alpha = 60°$, Structure 2 is placed almost out of the wake zone of Structure 1 and is subjected to a higher-velocity flow compared with other cases. Hence, a negative-pressure region with a higher amplitude than that with other α is formed behind Structure 2. Furthermore, the pressure on the front face of Structure 2 changes to be positive and its amplitude becomes larger with the increasing α, which leads to a positive drag force on Structure 2 as shown in Table 4.

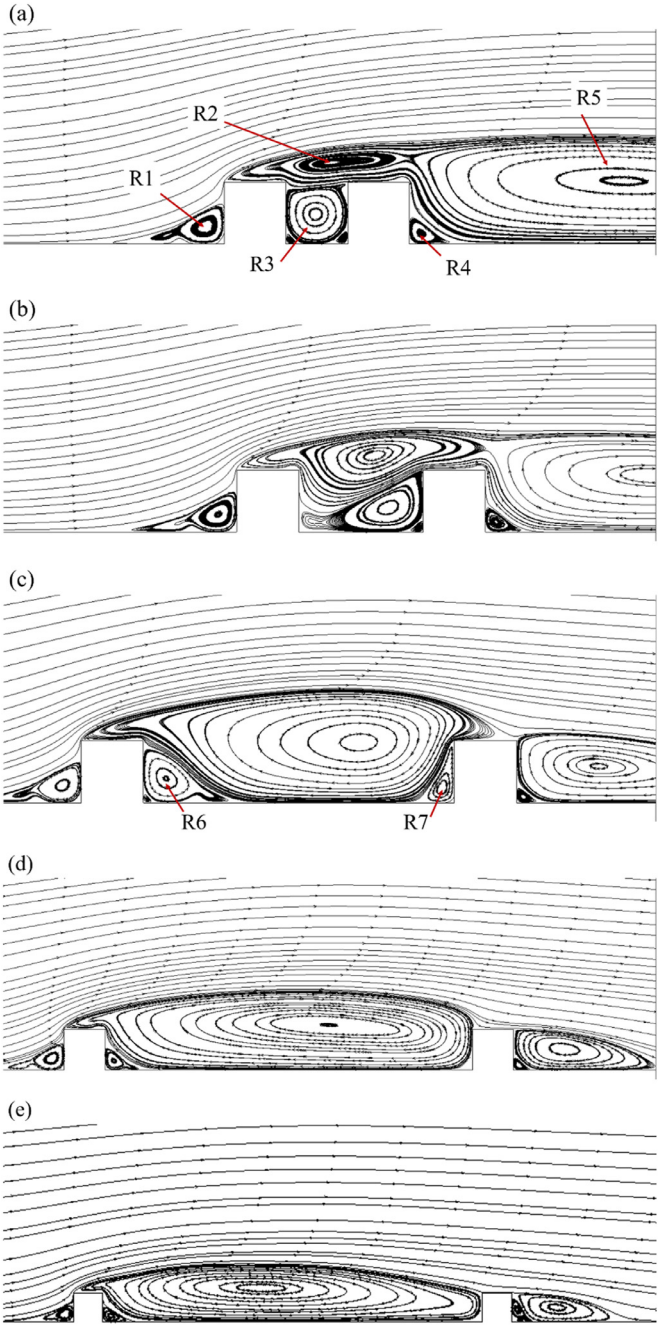

Fig. 13. Streamlines for wall-mounted squares in tandem with: (a) $G/D = 2$; (b) $G/D = 3$; (c) $G/D = 6$; (d) $G/D = 10$; (e) $G/D = 14$.

3.4. Horizontal velocity contours

The horizontal velocity contours for the wall-mounted squares in tandem with $G/D = 2$, 3, 6, 10 and 14 is presented Fig. 10. A high-speed velocity region is formed centered around $(x/D, y/D) \sim (5, 2)$ above the shear layer. It is obvious that with $G/D = 2 \sim 6$, the high-speed velocity region is squeezed and the amplitude of its core region is the largest with $G/D = 6$ among all G/D in the present study. Furthermore, with $G/D > 6$ the area of the high-speed velocity region is expanded with the increasing G/D.

The low-speed velocity region between the two squares is associated with the recirculation motions behind the separation point at the left top edge of Square 1. For $G/D = 2$, 3 and 6 the core of the low-speed velocity region is located close to the left top edge of Square 2. However, when $G/D > 6$ the core of the low-speed region is expanded and seems to be attached to the bottom wall.

The horizontal velocity contours for all α with $G/D = 6$ and 14 are presented in Figs. 11 and 12, respectively. It can be seen that both the amplitude and the area of the high-speed velocity decreases with the increasing α.

3.5. Streamlines around the structures in tandem

The streamlines around the two squares in tandem with different G/D are presented in Fig. 13. For $G/D = 2$ in Fig. 13(a), five main vortex motions denoted as R1∼R5 appears. A small vortex motions R1 is formed around the front face of Square 1 because the fluid particles hit Square 1 and flow down the bottom wall and the direction of the flow is reversed due to the bottom wall. The elongated R2 is located on top of the two tandem squares and induces R3 which is in a counterclockwise direction in the gap region between the two squares. At the back surface of Square 2, there is a large vortex R5 and it induces a small counterclockwise vortex R4 around the back corner of Square 2. The vorticities between the two squares varies with the increasing G/D. From $G/D = 2$ in Fig. 13(a) to $G/D = 3$ in Fig. 13(b), R2 starts to suppress R3 and becomes a larger vortex attached to the bottom wall with $G/D = 6 \sim 14$. The large vortex R2 induces two small vorticities denoted as R6 and R7, which are both in a counterclockwise direction and located around the back face of Square 1 and the front face of Square 2, respectively. The sizes of R6 and R7 are reduced significantly with the increasing G/D from 10 to 14. The size of the large vortex R5 behind Square 2 also decreases with the increasing G/D.

Figs. 14 and 15 show the streamlines for all trapezoidal configurations in tandem with $G/D = 6$ and 14, respectively. With $G/D = 6$, R7 almost disappears and R6 is suppressed with the increasing α. R2 seems to be attached to the front face of Structure 2 and the back face of Structure 1 as well as the bottom wall with $\alpha = 45°$, $60°$.

With $G/D = 14$, the recirculation motions behind the two structures become separated. The size of the large recirculation motion behind Structure 1 is reduced with the increasing α due to the low velocity around the separation point of the left top edge of Structure 1. For $\alpha = 60°$, the large recirculation motion behind Structure 1 seems to be detached from the front face of Structure 2. The flow separation takes place at the right top edge of Structure 2 and the recirculation motion behind Structure 2 is much smaller than that behind Structure 1.

4. Conclusion

In the present study, two-dimensional numerical simulations of turbulent boundary layer flows at $Re = 1.19 \times 10^5$ around two wall-mounted squares and trapezoidal structures in tandem have been carried out. The simulations are based on the RANS equations combined with the $k - \omega$ SST model. The effects of different incline angles of the two side slopes of the trapezoidal structures and the gap ratio G/D between the two structures on the hydrodynamic quantities for both structures have been investigated. Main conclusions can be outlined as follows:

(1) For the squares in tandem, $G/D = 6$ is found to be a critical value for the drag forces on the two square structures. The drag coefficient on Square 1, C_{D1} increases with G/D for $G/D < 6$ and decreases with G/D for $G/D > 6$. The drag coefficient on Square 2, C_{D2} is negative. The absolute value of C_{D2} increases with G/D for $G/D < 6$ and decreases with G/D for $G/D > 6$.
(2) The lift coefficients for the two squares are all positive. For Square 1, the lift coefficients C_{L1} increases with $G/D < 3$ and decreases with $G/D > 3$. The lift coefficients of Square 2, C_{L2} decreases with the increasing G/D.
(3) The amplitude of the negative pressure region between Square 1 and Square 2 increases with $2 < G/D < 6$ and decreases with

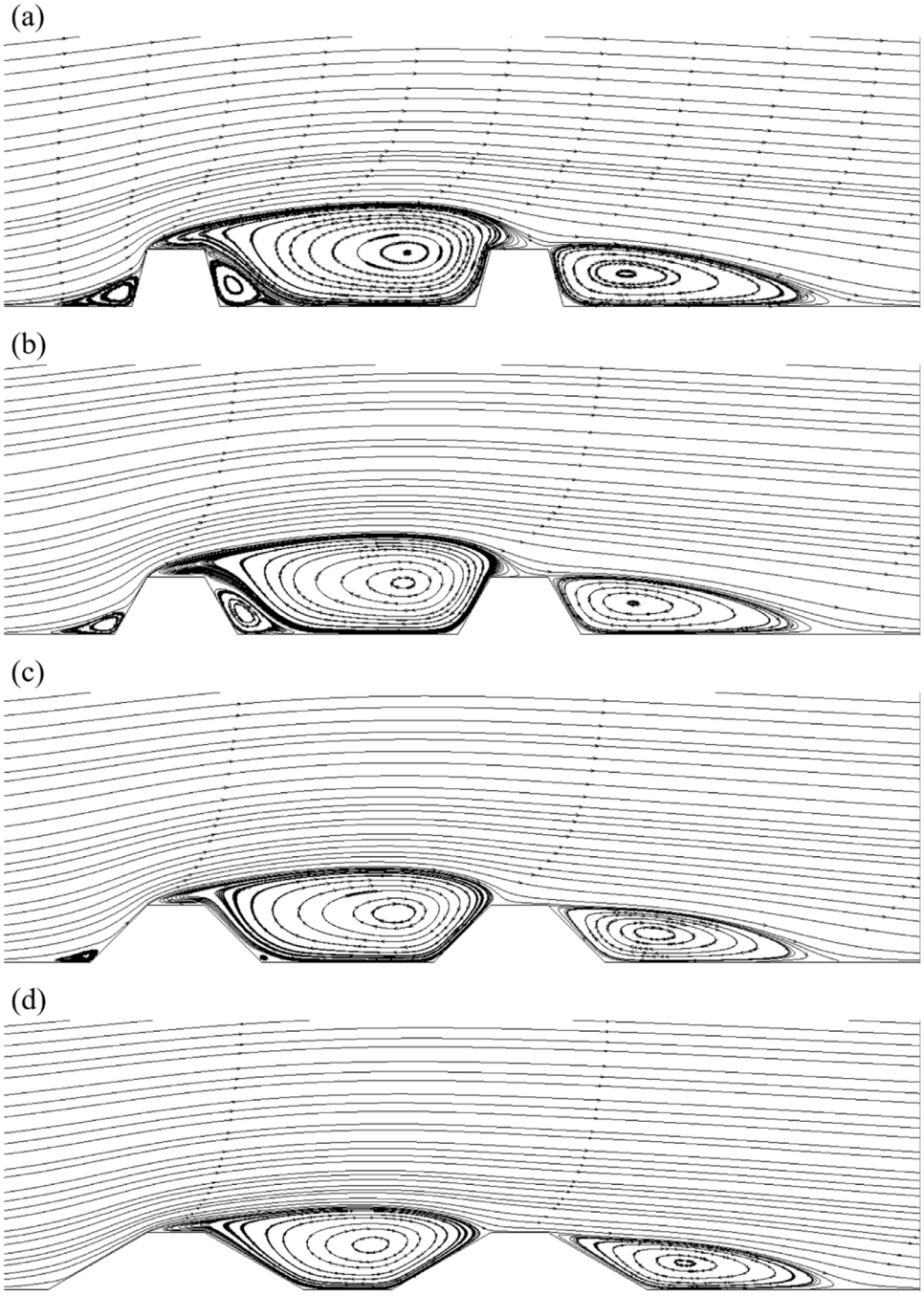

Fig. 14. Streamlines for $G/D = 6$ for varying trapezoidal configurations α: (a) 15°; (b) 30°; (c) 45°; and (d) 60°.

$6 < G/D < 14$.

(4) For trapezoidal structures, both the drag and lift coefficients for Structure 1, C_{D1} and C_{L1} decrease with the increasing α. The drag coefficient for Structure 2 changes from negative to positive with $G/D = 14$ for all $\alpha > 0^{\circ}$ The amplitude of the negative pressure region between Structure 1 and Structure 2 decreases with the increasing α.

CRediT authorship contribution statement

Guang Yin: Conceptualization, Methodology, Software, Validation, Formal analysis, Investigation, Writing - original draft, Writing - review & editing, Visualization. **Martin Andersen:** Methodology, Validation, Formal analysis, Investigation, Writing - review & editing, Visualization. **Muk Chen Ong:** Conceptualization, Investigation, Writing - review & editing, Resources, Supervision, Project administration, Funding acquisition.

Declaration of Competing Interest

The authors declare that they have no known competing financial interests or personal relationships that could have appeared to influence the work reported in this paper.

Acknowledgement

This study was supported with computational resources provided by the Norwegian Metacenter for Computational Science (NOTUR), under

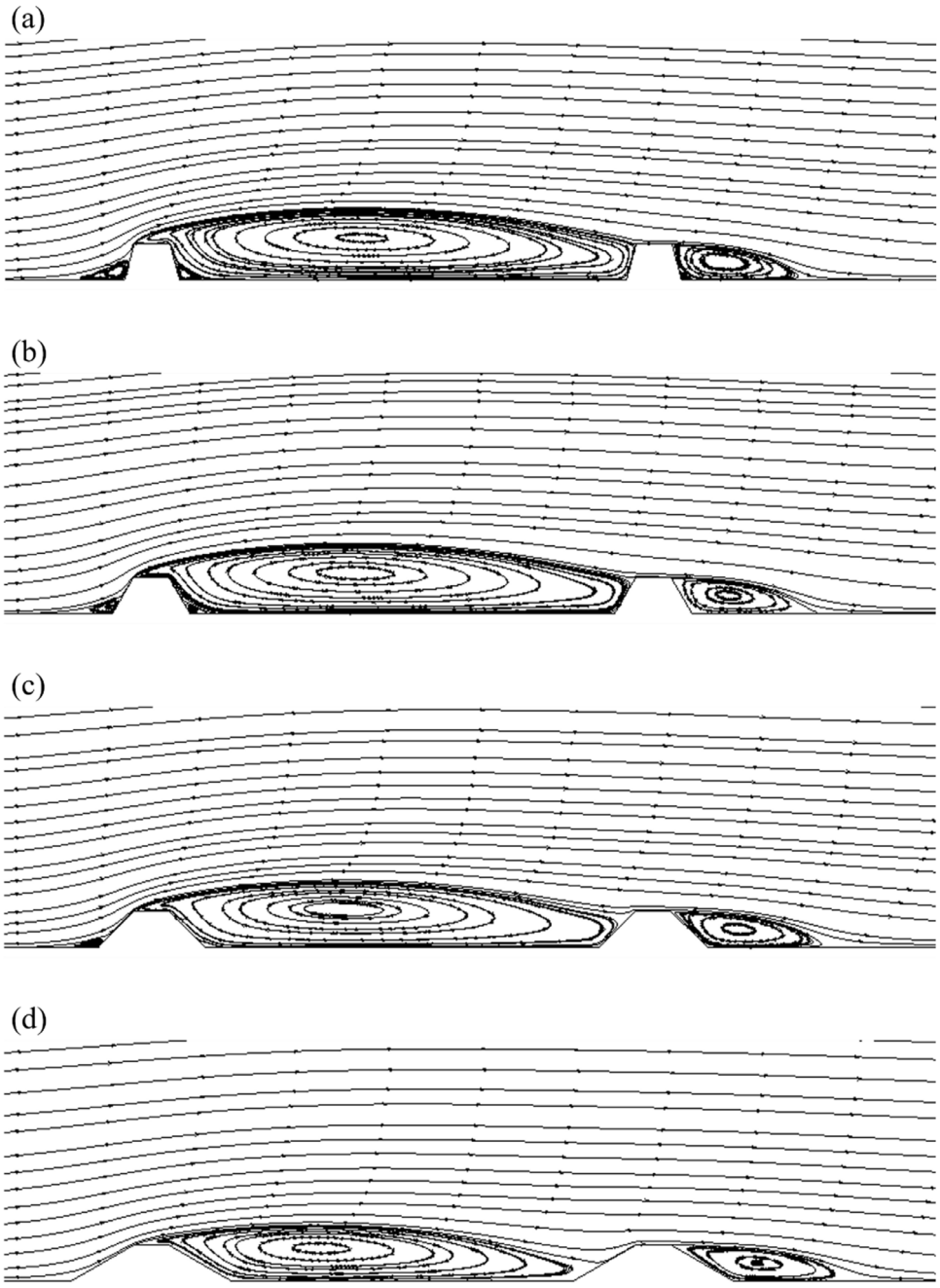

Fig. 15. Streamlines for $G/D = 14$ for varying trapezoidal configurations α: (a) 15˚; (b) 30˚; (c) 45˚; and (d) 60˚.

Project No: NN9372K.

References

[1] M. Arie, M. kiya, H. Tamura, M. Kosugi, K. Takaoka, Flow over rectangular cylinders immersed in a turbulent boundary layer: part 2 flow patterns and pressure distributions, Bull. JSME 18 (125) (1975) 1269–1276.
[2] R.W. Benodekar, A.J.H. Goddard, A.D. Gosman, R.I. Issa, Numerical prediction of turbulent flow over surface-mounted ribs, AIAA J. 23 (3) (1985) 359–366.
[3] G. Bergeles, N. Athanassiadis, The flow past a surface-mounted obstacle, J. Fluids Eng. 105 (4) (1983) 461–463.
[4] B. Brørs, Numerical modeling of flow and scour at pipelines, J. Hydraul. Eng. 125 (5) (1999) 511–523.
[5] D. Crabb, D. Durao, J. Whitelaw, Velocity characteristics in the vicinity of a two-dimensional rib, Proceeding of the 4th Brazilian Congress on Mechanical Engineering, Florianopolis, Brazil, 1977, pp. 47–58.
[6] Y. Dai, H. Wang, C. Tian, Numerical simulations of turbulent flow over two surface-mounted tandem square cylinders, Proceeding of the ASME 36th International Conference on Ocean, Offshore and Arctic Engineering, American Society of Mechanical Engineers, 2017pp. V07AT06A040-V07AT06A040.
[7] M.C. Good, P.N. Joubert, The form drag of two-dimensional bluff-plates immersed in turbulent boundary layers, J. Fluid Mech. 31 (3) (1968) 547–582.
[8] H. Gopalan, R. Jaiman, Numerical study of the flow interference between tandem cylinders employing non-linear hybrid URANS–LES methods, J. Wind Eng. Ind. Aerodyn. 142 (2015) 111–129.
[9] R.R. Hwang, Y.C. Chow, Y.F. Peng, Numerical study of turbulent flow over two--dimensional surface-mounted ribs in a channel, Int. J. Numer. Methods Fluids 31 (4) (1999) 767–785.
[10] W.P. Jones, B. Launder, The calculation of low-Reynolds-number phenomena with a two-equation model of turbulence, Int. J. Heat Mass Transf. 16 (6) (1973) 1119–1130.
[11] Z. Li, M.A. Prsic, M.C. Ong, B.C. Khoo, Large Eddy simulations of flow around two circular cylinders in tandem in the vicinity of a plane wall at small gap ratios, J. Fluids Struct. 76 (2018) 251–271.
[12] Y.Z. Liu, F. Ke, H.J. Sung, Unsteady separated and reattaching turbulent flow over a two-dimensional square rib, J. Fluids Struct. 24 (3) (2008) 366–381.
[13] R. Martinuzzi, C. Tropea, The flow around surface-mounted, prismatic obstacles placed in a fully developed channel flow, Trans. Am. Soc. Mech. Eng. J. Fluids Eng. 115 (1993) 85.

[14] F.R. Menter, Two-equation eddy-viscosity turbulence models for engineering applications, AIAA J. 32 (8) (1994) 1598–1605.
[15] M.C. Ong, T. Utnes, L.E. Holmedal, D. Myrhaug, B. Pettersen, Numerical simulation of flow around a circular cylinder close to a flat seabed at high Reynolds numbers using a k–ε model, Coast. Eng. 57 (10) (2010) 931–947.
[16] J. Paik, F. Sotiropoulos, F. Porté-Agel, Detached eddy simulation of flow around two wall-mounted cubes in tandem, Int. J. Heat Fluid Flow 30 (2) (2009) 286–305.
[17] M.A. Prsic, M.C. Ong, B. Pettersen, D. Myrhaug, Large Eddy simulations of flow around a circular cylinder close to a flat seabed, Mar. Struct. 46 (2016) 127–148.
[18] M.A. Prsic, M.C. Ong, B. Pettersen, D. Myrhaug, Large Eddy simulations of flow around tandem circular cylinders in the vicinity of a plane wall, J. Mar. Sci. Technol. 24 (2) (2019) 338–358.
[19] D.N. Ryu, D.H. Choi, V.C. Patel, Analysis of turbulent flow in channels roughened by two-dimensional ribs and three-dimensional blocks. Part I: resistance, Int. J. Heat Fluid Flow 28 (5) (2007) 1098–1111.
[20] M.A. Tauqeer, Z. Li, M.C. Ong, Numerical simulation of flow around different wall-mounted structures, Ships Offshore Struct. 12 (8) (2017) 1109–1116.
[21] X.K. Wang, Z. Hao, J.X. Zhang, S.K. Tan, Flow around two tandem square cylinders near a plane wall, Exp. Fluids 55 (10) (2014) 1818.
[22] D.C. Wilcox, Turbulence Modeling For CFD (Vol. 2, pp. 172-180). La Canada, DCW industries, CA, 1998.
[23] D.L. Young, T.I. Eldho, J.T. Chang, Large eddy simulation of turbulent flows in external flow field using three-step FEM–BEM model, Eng. Anal. Bound. Elem. 30 (7) (2006) 564–576.
[24] F.R. Menter, M. Kuntz, R. Langtry, Ten years of industrial experience with the SST turbulence model, Turbul. Heat Mass Transfer 4 (1) (2003) 625–632.